nature communications

Article

https://doi.org/10.1038/s41467-026-69783-5

# Climate models exaggerate greenhouse gas impact on recent interhemispheric temperature patterns and tropical climate

Received: 27 May 2025

Accepted: 10 February 2026

Published online: 27 February 2026

Check for updates

Chengfei He[1,2,3] ✉, Amy C. Clement[3], Mark A. Cane[4], Alex Gonzalez[2], Young-Oh Kwon[2], Jia-Rui Shi[5], Jeremy M. Klavans[3] & Lisa N. Murphy[3]

The interhemispheric thermal contrast, defined as the mean sea surface temperature difference between the northern and southern hemispheres, crucially influences tropical climate. Climate models show a positive interhemispheric thermal contrast trend since 1950, with more warming in the northern hemisphere compared to the southern hemisphere, contradicting the observed negative trend. Here we show this discrepancy stems from models overestimating greenhouse gas responses via wind-evaporation-sea surface temperature feedback, while anthropogenic and natural aerosols combine to produce the negative trend in observations. Consequently, models with high equilibrium climate sensitivity exhibit larger discrepancies with observations. Despite model failure to reproduce the trend, the modeled multidecadal interhemispheric thermal contrast variability aligns with observations, enabling a constrained estimate of effective radiative forcing due to aerosol-cloud interactions of $-0.6 \pm 0.3 W/m^2$, with a "likely" range 57% narrower than the latest IPCC report. Our study further suggests that future northward shifts of the tropical rain belt are likely to be less pronounced than predicted by climate models with high equilibrium climate sensitivity.

The interhemispheric thermal contrast (IHTC) − the Northern Hemisphere (NH) mean sea surface temperature (SST) minus the Southern Hemisphere (SH) mean SST − is one of the dominant modes of global SST variability[1,2]. The IHTC imposes energetic constraints on the Hadley circulation in the tropics[2–4] and storm tracks in the extratropics[5], which in turn impact billions of people through their influence on various aspects of the global hydrological cycle. Understanding the factors that affect the IHTC and its sensitivity to perturbations in natural and anthropogenic sources can improve projections of future changes.

Accurately simulating the IHTC remains a significant challenge for climate models. While current state-of-the-art climate models simulate global mean SST reasonably well[6], the same models struggle to replicate the observation when calculating the IHTC, the hemispheric contrast, over the past century[7,8]. Notably, our recent study[9] reveals that models in Coupled Model Intercomparison Project Phase 6 (CMIP6) exhibit a systematically positive trend in IHTC that contradicts observations, though the underlying mechanism remains unknown.

The model-data difference in IHTC could stem from differences in the model response to external forcing and internal variability, particularly internal atmospheric and oceanic variability not captured in uninitialized CMIP6 model simulations. For example, coordinated paleoclimate proxies and numerical experiments suggest that IHTC changes in past climates were mainly driven by variability in the Atlantic meridional overturning circulation (AMOC)[10,11]. During 1960-1970s, a large influx of freshwater from the Arctic Ocean led to a salinity anomaly in the subpolar North Atlantic, known as the "Great Salinity Anomaly", which weakened the deep water formation and

[1]Department of Marine and Environmental Sciences, Marine Science Center, Northeastern University, Nahant, MA, USA. [2]Woods Hole Oceanographic Institution, Woods Hole, MA, USA. [3]Rosenstiel School of Marine, Atmospheric, and Earth Science, University of Miami, Miami, FL, USA. [4]Lamont-Doherty Earth Observatory of Columbia University, Palisades, NY, USA. [5]Courant Institute, New York University, New York, NY, USA. ✉e-mail: ch.he@northeastern.edu

potentially the AMOC[12], coinciding with an abrupt decrease in the IHTC[13,14].

In addition to internal variability, the IHTC change could be driven by various external forcings. In response to greenhouse gases (GHG), climate models suggest that the NH warms faster than the SH due to the land-ocean fraction difference[15,16], the asymmetry of sea ice variability between the Arctic and the Antarctic[17–19], and delayed warming in the Southern Ocean poleward of 50°S[20,21]. Additionally, anthropogenic aerosols (AER), predominantly emitted in the NH, are expected to have a greater cooling effect there compared to the SH, which causes an energy imbalance between hemispheres and shifts the tropical rain belt southward[7,22–27]. However, the cooling effect induced by AER can be offset by warming due to GHG, resulting in a nuanced net effect[1]. Though insightful, these findings are mainly based on climate models, which have various known biases in physical processes and radiative feedbacks[28–32]. As such, we hypothesize that discrepancies between climate models and real-world observations in IHTC and associated tropical climate can thus arise from differences in their sensitivities to external forcings, particularly since World War II when anthropogenic forcings have been strong.

Recent studies have improved our understanding of the climatological IHTC bias in CMIP6 models[32]. In this paper, we investigate factors influencing the transient IHTC since 1950 and address discrepancies between model simulations and observed data. We begin by analyzing statistics, decomposing the IHTC into a linear long-term trend and multidecadal variability to identify drivers of the recent IHTC variability and to uncover clues in the systematic differences between models and data. We conclude by examining the physical processes responsible for the IHTC pattern and the model-data discrepancies. We will show that current climate models reasonably simulate the multidecadal IHTC variability as a response to AER and natural forcings (NAT, such as solar activities and volcanic eruptions), but the modeled long-term trend is proportional to each model's sensitivity to GHG due to wind-evaporation-SST (WES) feedback[33,34] that results in systematic model-data differences in IHTC and its tropical impacts. The consistency between modeled and observed multidecadal IHTC provides observationally-constrained estimates of the real-world effective radiative forcing due to aerosol-cloud interactions (ERFaci, $-0.6 \pm 0.3 W/m^2$). However, the discrepancy in long-term trend worsens in models with high equilibrium climate sensitivity (ECS), implying that the real-world ECS may be low[35,36].

## Results

### Systematic bias in SST and tropical climate in CMIP6 models

Building on our previous work[9], we begin by revisiting the comparison of simulated post-1950 IHTC with observations in a larger CMIP6 ensemble, which confirms a systematic bias in the IHTC and tropical climate in current state-of-the-art climate models. Fig. 1a depicts the SST trend in the ensemble mean of 542 CMIP6 historical simulations from over 50 models (Supplementary Data. 1). The ensemble mean is an excellent approximation to the response to external forcings (e.g., GHG, AER, and NAT), as independent representations of internal climate variability in different members are largely cancelled out in the mean through averaging. The ensemble mean shows an enhanced warming in the North Atlantic and North Pacific. As a result, the SST trend between the NH and SH exhibits a positive difference. However, Fig. 1b shows that the observations are the opposite. The real world shows a relative cooling trend in parts of the North Pacific and Atlantic and a warming trend in most of the SH since 1950. The model-data difference is even more striking in Fig. 1c, which highlights that the modeled SST in the NH warmed faster than observed, whereas it warmed slower than observed in the SH. We examine the time series of the IHTC in Fig. 1f. The IHTC is defined as the mean SST difference between NH[0–60 °N] and SH[40 °S-0], which maximizes quality data coverage while capturing the primary zones of hemispheric asymmetry. We exclude the Southern Ocean (south of 40°S) to avoid regions with sparse pre-satellite observations that may confound the temperature signal. The observations indicate an overall decreasing trend in IHTC with strong multidecadal variability, while the modeled IHTC largely shows a positive trend on top of the multidecadal variability. Fig. 1g summarizes the trend in IHTC for simulations and observations, showing that simulations consistently exhibit a higher trend. In fact, the observations fall in ~1st percentile of the model distribution. We also verified that the IHTC based on the SST difference between [0–60°N] and [60°S–0] show quantitatively consistent results (Supplementary Fig. 1).

Interestingly, the model-observation surface temperature discrepancy only shows up in the interhemispheric SST, as the simulated interhemispheric land surface temperature contrast aligns well with observations and exhibits a response larger in magnitude than the SST contrast (Supplementary Fig. 2). However, slight changes in the interhemispheric SST difference can have dramatic climate impacts in the tropics. In both model and observations, a positive IHTC excites an anomalous Hadley Circulation (HC) in the tropics, which boosts (suppresses) upward motion in the NH (SH) and therefore causes a northward shift of the Intertropical Convergence Zone (ITCZ)[4] (Supplementary Fig. 3). Figure 1d, e underscore the differences in tropical climate between the model and observations, attributed to differences in the IHTC. In the model, the cross-equatorial anomalous HC (see Methods: Definition) is strongly anticorrelated with the IHTC (Fig. 1d), which transports energy to the SH (Supplementary Fig. 3b). Consequently, the intertropical precipitation contrast, as a measure of the ITCZ change (refs. 22,25, see Methods: Definition), is positively correlated with the IHTC, indicating a northward shift of the ITCZ. The observed HC and ITCZ also covary with the IHTC, showing an overall trend opposite to that of the model simulation. Note that the observed IHTC is less correlated with the ITCZ than the Hadley Circulation, particularly after the 2000s. This is probably due to the ITCZ calculation relying on land-station precipitation, which is typically noisier but provides observational data prior to the satellite era[37].

### Largely forced observed IHTC

Given the observed IHTC is around the 1st percentile of the model distribution (Fig. 1g), the model-data difference is highly unlikely to be attributable to internal variability[22], which is further confirmed by considering distributions of the 65-year trends from CMIP6 pre-industrial control simulations (Supplementary Fig. 4). Therefore, the observed IHTC trend is most likely driven by external forcings, and we further hypothesize that the multidecadal variability of IHTC is also due to the external forcings. To show this, we regress the IHTC onto IHTCs calculated from the single forcing runs:

$$IHTC = \beta_{GHG} IHTC_{GHG} + \beta_{AER} IHTC_{AER} + \beta_{NAT} IHTC_{NAT} + \epsilon \quad (1)$$

in which the IHTC on the left-hand side of the equation is either from observations or CMIP6 all-forcing historical simulations. Equation 1 assumes the timing of IHTC variability is well simulated in single-forcing runs and nonlinear interactions between forcings are small. As such, linearly scaling and summing single-forcing IHTCs could reproduce the observed IHTC, provided that the observation is primarily driven by external forcings. The potentially muted amplitude of the forced responses in simulations due to low signal-to-noise ratio in large ensembles[9,38] would be compensated by the scaling factor, $\beta s$, when Eq.1 is applied to the observed IHTC.

We first verify this approach by regressing the forced IHTC in CMIP6 (blue curve in Fig. 1f). Fig. 2 legend indicates that the regression closely replicates the forced IHTC in the simulation, with an $R^2$ value approaching 1. The ability of the linear Eq. (1) to fully capture all forcings IHTC response indicates that any nonlinear interactions among

https://doi.org/10.1038/s41467-026-69783-5

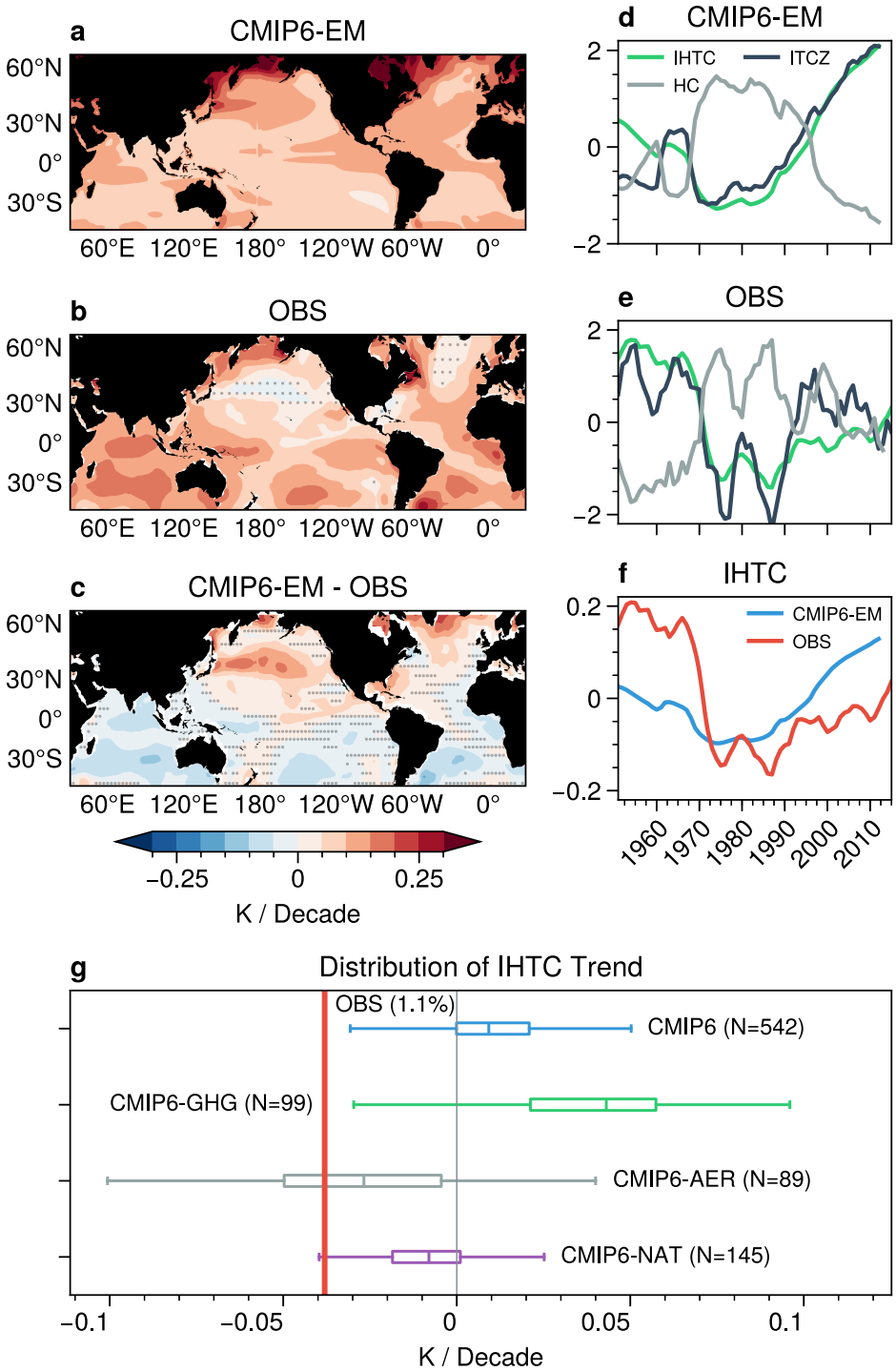


**Fig. 1 | Systematic biases in sea surface temperature (SST) and tropical climate in the Coupled Model Intercomparison Project Phase 6 (CMIP6) simulations from 1950 to 2014. a** SST trend of the ensemble mean of CMIP6 simulations; **b** the same as **a**, but for observations (ERSSTv5); **c** difference between (**a** and **b**). Regions that are not statistically significant at the 95% confidence level according to Student's t-test are stippled in (**a**–**c**). **d** Time series of normalized interhemispheric thermal contrast (IHTC, green), Intertropical Convergence Zone (ITCZ, black), and cross-equatorial Hadley circulation (HC, gray) in the CMIP6 ensemble mean; **e** same as **d**, but for observations (20$^{th}$ reanalysis and GPCC). **f** Time series of IHTC in both CMIP6 ensemble mean and observations, with units in K. A 7-yr running mean has been applied to time series in **d**–**f** for presentation. **g** Boxplot depicting the distribution of IHTC trends in CMIP6 all-forcing and single-forcing runs, where the edges of the box indicate the first and third quartiles and the whiskers extend to the most extreme data point within 1.5 times the interquartile range. 'N' denotes the ensemble size for each simulation. The observational trend is represented by the red line (ERSSTv5), which is at the ~1st percentile of the CMIP6 simulations. HadISST and COBE2 are at ~3$^{rd}$ percentile. See methods and main text for the definition of IHTC, ITCZ, and HC.

the individual forcings are negligible. The regressions for observations also show large $R^2$ values, above 0.8 for Hadley Centre Sea Ice and Sea Surface Temperature (HadISST) and Centennial in situ Observation-Based Estimates 2 (COBE2), and 0.9 for the Extended Reconstructed Sea Surface Temperature v5 (ERSSTv5) (See Methods: Observations). This regression result indicates a substantial impact (at least 80%) of the external forcing on the observed IHTC evolution[7].

Given that the observed IHTC is mainly driven by external forcings, we further hypothesize that the model-data discrepancy arises from differences in their SST sensitivities to these forcings. The scaling

https://doi.org/10.1038/s41467-026-69783-5

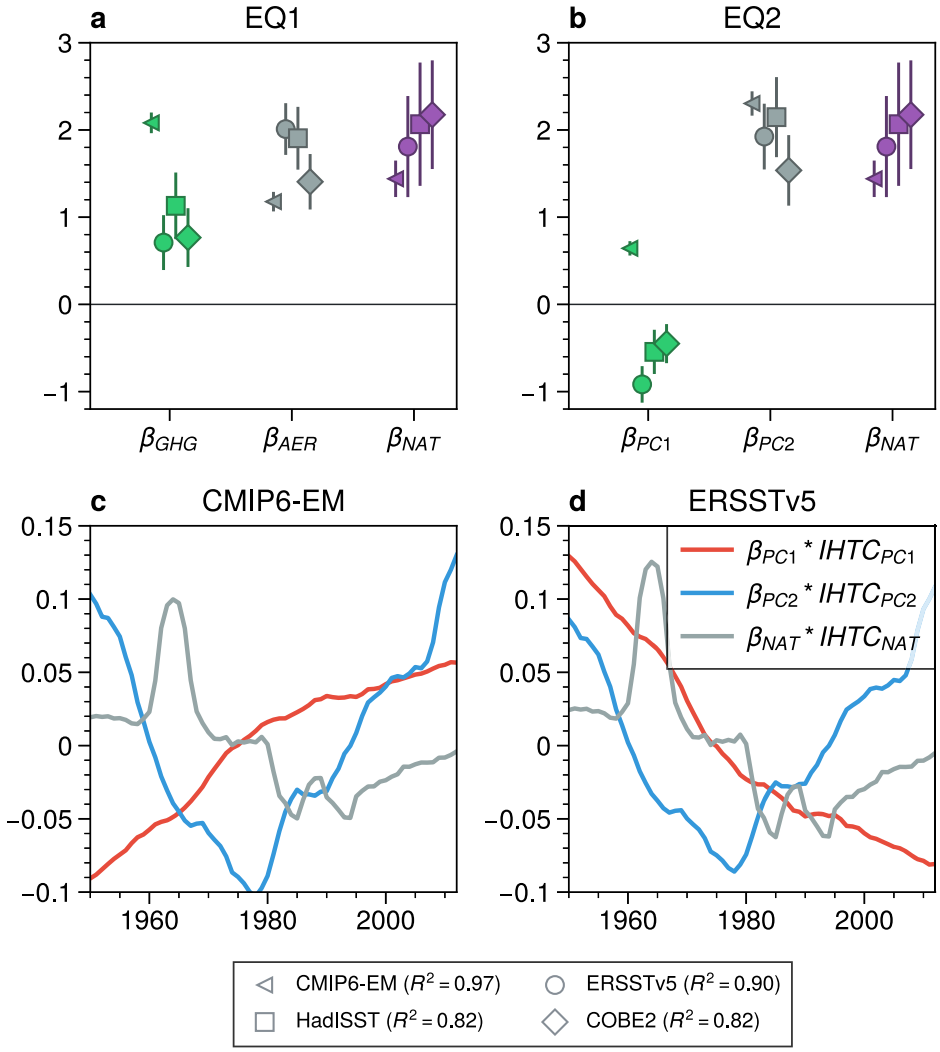


**Fig. 2 | Regression scaling factors and temporal decomposition of interhemispheric thermal contrast (IHTC) contributions in both observation and CMIP6-EM in Eqs. 1 and 2. a** Scaling factors for Eq. 1; **b** Scaling factors for Eq. 2. Marker colors indicate different scaling factors in Eqs. 1 and 2 (see x-label). The $R^2$ values for the regression of CMIP6 model ensemble mean and observations are indicated in the legend at the bottom. Whiskers denote the 95% confidence interval. **c** temporal decomposition of the regression in Eq. 2 for CMIP6-EM (Unit: K). **d** as in **c**, but for ERSSTv5. Red, blue, and gray lines represent contributions from $IHTC_{PC1}$, $IHTC_{PC2}$, and natural forcing, respectively.

factors, $\beta s$, in Fig. 2a, illustrate these sensitivities. For the CMIP6 models, the contribution by GHG is nearly twice as large as AER, while the opposite is the case for observations. That is, the modeled IHTC is overly sensitive to the GHG and too muted in response to AER. This raises the next question: Is the bias primarily caused by sensitivity to GHG, AER, or both? The regression based on Eq. 1 cannot provide the answer due to the high collinearity between the modeled IHTCs in GHG and AER runs (with a correlation of -0.75, Supplementary Fig. 5a), which complicates the interpretation of the relative roles of predictors in the regression.

### Exaggerated role of GHGs in modeled IHTC

To eliminate the collinearity between the $IHTC_{GHG}$ and $IHTC_{AER}$, we perform Principal Component Analysis (PCA) on them, which converts them into two orthogonal modes: $IHTC_{PC1}$ and $IHTC_{PC2}$ (See Methods: PCA). The first PC, $IHTC_{PC1}$, represents a nearly linear trend mode due to the long-term changes in GHG (positive) and AER (negative, Supplementary Fig. 5c), which resembles the leading mode of radiative forcing identified by spatial-temporal analysis in recent studies[39–41]. The second PC, $IHTC_{PC2}$, represents multidecadal variability dominated by AER (Supplementary Fig. 5d). Now, we regress the modeled and observed IHTC onto the PCs and $IHTC_{NAT}$ again:

$$IHTC = \beta_{PC1} IHTC_{PC1} + \beta_{PC2} IHTC_{PC2} + \beta_{NAT} IHTC_{NAT} + \epsilon \quad (2)$$

Figure 2b presents scaling factors for Eq. 2, where the $R^2$ values remain unchanged. The $\beta_{PC2}$ and $\beta_{NAT}$ for model and observation are consistent within the observational uncertainty, suggesting the AER-induced multidecadal and the NAT-induced IHTC are consistent between model and observation[7,22–26,42]. However, the modeled $\beta_{PC1}$ has the opposite sign as the observed, suggesting the major model-data difference originates from this mode. The individual timeseries of the three terms in Eq. 2 for model and observation are shown in Fig. 2c, d. The major model-data difference lies in the $\beta_{PC1} IHTC_{PC1}$. The positive $\beta_{PC1}$ implies that the long-term trend in IHTC is dominated by GHG in the model, while the negative $\beta_{PC1}$ in the observation suggests the long-term trend in observed IHTC is dominated by AER. The combined $IHTC_{PC2}$ and $IHTC_{NAT}$ account for more than 65% of the total variance in observations, suggesting that the real world is remarkably influenced by the AER and NAT. Notably, the abrupt cooling in the observed IHTC in 1960-1970s is substantially impacted by the Mount Agung volcanic eruptions in NAT[22] (Fig. 2d, gray curve). After 1980, the

https://doi.org/10.1038/s41467-026-69783-5

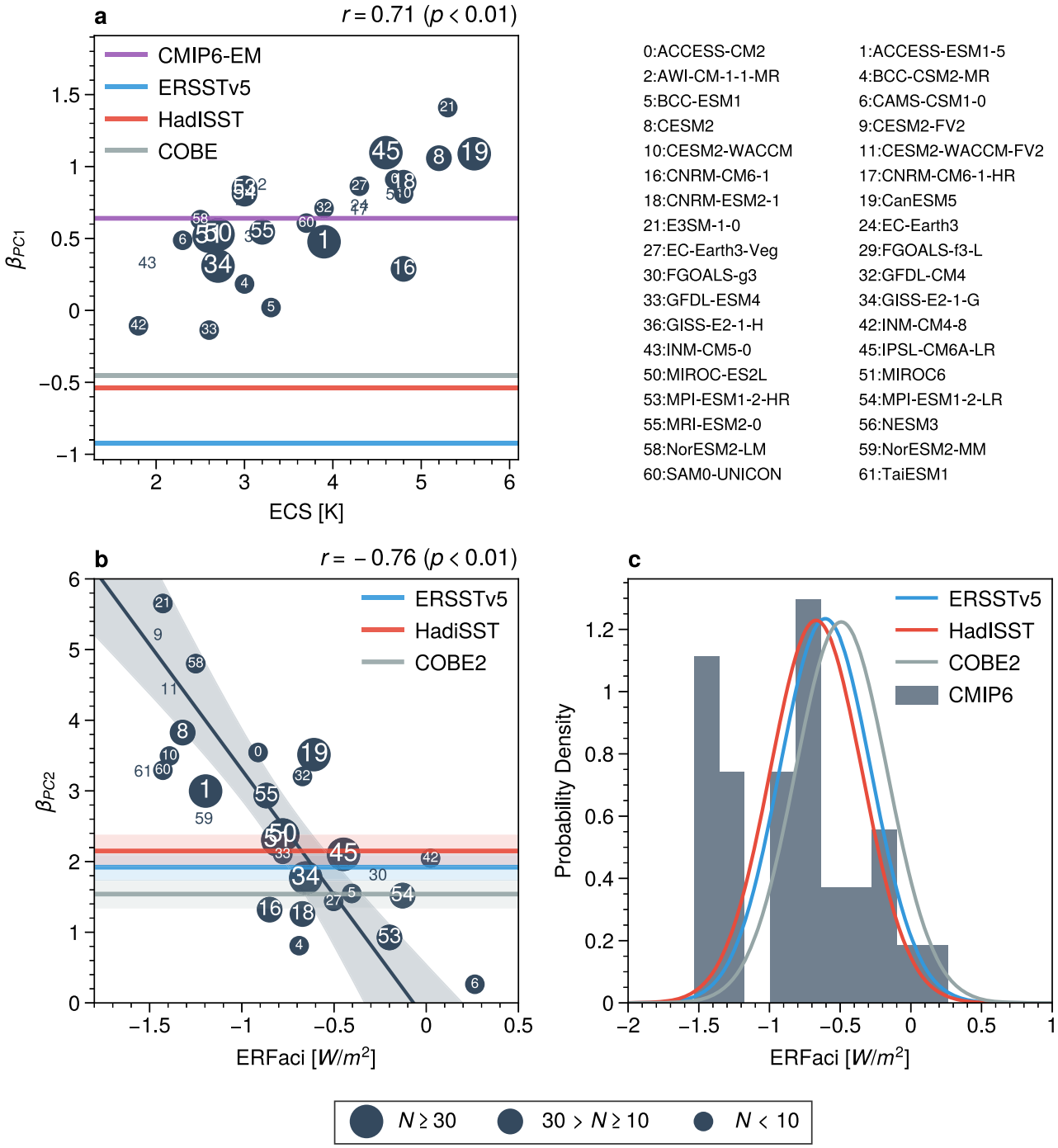


**Fig. 3 | Relationship between long-term trends and multidecadal variability in the Coupled Model Intercomparison Project Phase 6 (CMIP6) models' inter-hemispheric thermal contrast (IHTC) with their sensitivity to greenhouse gases (GHG) and anthropogenic aerosols (AER). a** scatterplot showing the inter-model relationship between $\beta_{PC1}$ and equilibrium climate sensitivity (ECS). **b** scatterplot between $\beta_{PC2}$ and effective radiative forcing due to aerosol-cloud interactions (ERFaci). **c** probability density function for ERFaci in both models and observations. In **b**, the solid dark line represents the best-fit linear regression of ERFaci on $\beta_{PC2}$ across the model ensemble, with prediction error indicated by dark shadings. Horizontal lines denote the best-estimated $\beta_{PC2}$ from various observations, with shading indicating one standard deviation. Numbers within each symbol correspond to individual CMIP6 models as listed in the legend. Models are divided into two groups: those with ECS and ERFaci available (circled) and those with either ECS or ERFaci (non-circled). Circle sizes are proportional to each model's ensemble size (legend). Correlations in **(a)** and **(b)** are calculated using circled models, and they remain almost the same if including non-circled models. The associated p-values are presented.

observed IHTC shows a positive trend mostly driven by the multidecadal variability of the AER (Fig. 2d, blue curve), consistent with a dipole SST mode identified in a recent fingerprint analysis[23].

Figure 3 extends the above analysis to each single-model ensemble in CMIP6 to investigate model-to-model spread. We calculate the ensemble average of each model's IHTC and then perform a regression using Eq. 2. Since PC1 represents a combined AER and GHG effect in the long-term IHTC trend, we scatterplot $\beta_{PC1}$ of each model against its ECS and ERFaci as proxies for the response/sensitivity to GHG and AER, respectively, to investigate the controlling factor for the model spread. The $\beta_{PC1}$ and ECS show a clear linear relationship, indicating that models with high ECS tend to produce a high IHTC trend in the

https://doi.org/10.1038/s41467-026-69783-5

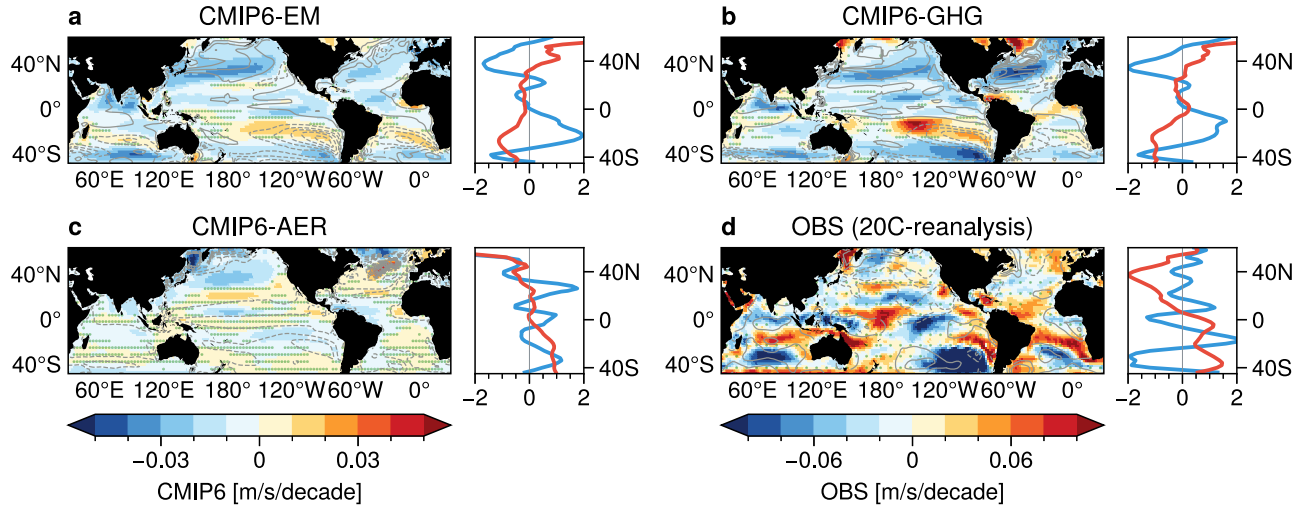


**Fig. 4 | Wind-Evaporation-Sea surface temperature (WES) feedback in the in the Coupled Model Intercomparison Project Phase 6 (CMIP6) simulations. a** left panel: trend of surface wind speed (shading) and Sea surface temperature (SST, contour) in the CMIP6 simulations; right panel: normalized zonal mean of the surface wind speed (blue) and SST (red) trends. **b**–**d**, as in (**a**), but for GHG, AER runs, and observations, respectively. The relatively warm areas are in solid contours, and the relatively cold areas are in dashed contours. Contour intervals are 0.02 K for **a**–**c** and 0.04 K for (**d**). Note that the colorbar scales for the observation and CMIP6 runs differ. Regions that are not statistically significant at the 95% confidence level according to Student's t-test are stippled for the trend of surface wind speed.

historical period (Fig. 3a). The ERFaci is less correlated with the $\beta_{PC1}$ and combining ECS and ERFaci doesn't improve their correlation with the $\beta_{PC1}$ either (Supplementary Fig. 6a, c). This implies that, in contrast to the observed IHTC, the systematic positive trend in IHTC of CMIP6 models largely results from their response to GHG. It should be noted that ECS and ERFaci are correlated to some extent in CMIP6 models[35,43] (Supplementary Fig. 6a, c).

In contrast, the multidecadal variability in IHTC is regulated by AER, consistent with the observations[23,39,44]. As shown in Fig. 3b, the $\beta_{PC2}$ and ERFaci are well correlated, and the observation is within the model spread. This implies models with strong ERFaci tend to produce a strong multidecadal variability in IHTC. Though ECS and $\beta_{PC2}$ show a moderate correlation (Supplementary Fig. 6b), combining ECS and ERFaci does not show any improvement in correlation compared to Fig. 3b. In short, the modeled multidecadal variability in IHTC is predominantly influenced by AER, aligning with observations. Conversely, the modeled long-term trend in our analysis period is primarily driven by GHG, contradicting the observed IHTC that is driven by AER and NAT.

## IHTC shaped by WES feedback

The strong correlation between ECS and $\beta_{PC1}$ suggests that the discrepancies between models and observations are linked to modeled SST responses to GHG. Energy budget analysis (see Methods: Energy budget analysis for SST trend) indicates that the trend of interhemispheric SST difference in the GHG run is primarily driven by turbulent heat flux, resulting in a positive SST difference between the NH and the SH. Radiative heat fluxes exhibit largely uniform SST response in the two hemispheres, while ocean dynamics produce a negative SST difference between the NH and SH (Supplementary Fig. 7). In mid- and high latitudes of the NH, the amplified air-sea temperature difference enhances turbulent heat uptake and thus warms the ocean surface (Supplementary Fig. 7e, f). In the tropics and subtropics, the SST pattern is regulated by the surface wind speed due to the wind-evaporation-SST (WES) feedback (Supplementary Fig. 7e, also see Fig. 2 in ref. 34).

The all-forcing CMIP6 surface wind and SST response is dominated by the GHG, rather than the AER (Fig. 4a–c). The WES feedback is more evident in Fig. 4a, which plots the forced trend of surface wind speed with overlaid contours representing SST trend in CMIP6 runs. Areas with reduced wind strength exhibit a relatively warmer SST pattern (solid contours), whereas areas with intensified wind display a relatively colder SST pattern (dashed contours). Mechanistically, weaker winds reduce evaporation, leading to less turbulent heat flux being removed from the ocean surface, thereby causing a warming anomaly; and vice versa. The WES feedback is even more apparent in the zonal mean profile, where wind speed and SST trends are normalized and show a mostly anticorrelated relationship in tropics and subtropics (Fig. 4a, b, right panel). Previous studies explicitly confirmed the role of the WES-feedback using a partial coupling experiment[33], in which the SST change induced by the WES feedback resembles the SST pattern in our CMIP6 GHG runs (Fig. 4e in ref. 33 vs. Fig. 4b contours in the present manuscript).

In addition to the ensemble mean of CMIP6, we further analyze the model spread of the IHTC in relation to the interhemispheric surface wind speed contrast (IHWC, see methods: Definition) and the air-sea temperature difference in mid-to-high latitudes [40–60°N] of the NH for 51 models. Supplementary Fig. 8a displays that the trends of IHTC and IHWC are well correlated. Most CMIP6 models exhibit a decreasing trend in IHWC and, consequently, an increasing trend in IHTC, which contradicts the observed negative IHTC trend (Figs. 1g and 3a). However, the relationship between the trend of IHTC and air-sea temperature difference is weaker (Supplementary Fig. 8b). In summary, while both surface wind speed and air-sea temperature difference contribute to the rising trend in the ensemble mean IHTC of CMIP6, surface wind speed has a greater impact on the spread of CMIP6 model results.

The SST trends in AER runs and observations are also substantially impacted by the WES feedback. However, the wind-SST relationship is not readily apparent in the AER and observation due to substantial multidecadal variability in surface wind speed, which may yield different outcomes in the linear trend (Fig. 4c and d). Supplementary Fig. 9 shows the trends in surface wind speed and SST in periods pre- and post-1980 in response to AER, which are anticorrelated between them across the global oceans. Note that the SST and surface wind speed trends are positively correlated in the subpolar North Atlantic, resulting from an enhanced AMOC that delays the formation of the warming hole in the model compared to observations[45].

Supplementary Fig. 10 illustrates similar wind-SST relationship for the observation in both periods, though the observed wind and SST are less correlated in the pre-1980 period. The weakened correlation between wind and SST may result from less reliable sea level pressure observations in the early period, impacting the assimilation of surface wind speed[46]. However, the pre-1980 observed SST pattern closely resembles the AER-induced SST pattern (Supplementary Figs. 10b and 9b). This confirms the observed IHTC is dominated by AER and NAT (Fig. 2d), possibly through the WES feedback (Supplementary Fig. 9a, b).

### Implications for ECS and ERFaci

Given the model's ERFaci and IHTC multidecadal variability are well correlated, we apply emergent constraints based on their linear relationship to estimate the real-world ERFaci. The estimated ERFaci is $-0.60 \pm 0.29 W/m^2$ ($1\sigma$, based on ERSSTv5), $-0.67 \pm 0.30 W/m^2$ (HadISST), and $-0.49 \pm 0.30 W/m^2$ (COBE2) (Fig. 3b, c). These estimates are less negative than the latest IPCC report[6] of $-1.0 \pm 0.7 W/m^2$, but are consistent with a recent estimation after assessing the actual impact of aerosols on cloud droplet number concentrations[47]. This difference in the mean value is likely caused by the overall less negative model's ERFaci in the present study. We obtain these CMIP6 ERFaci estimates from Wang et al.[35]. and project them onto Smith et al.'s estimates[48] due to their high covariance, since ERFaci estimated by Wang et al. is substantially lower (less negative) than those by Smith et al. To verify robustness, we also calculate emergent constraints using ERFaci from Smith et al. This constraint does produce more negative estimates for the ERFaci (Supplementary Fig. 11), though the correlation between ERFaci and $\beta_{PC2}$ is slightly reduced, from -0.76 to −0.63 ($p < 0.03$), probably due to fewer samples. On the other hand, our estimates consistently reduce uncertainty in the ERFaci. Relative to the 'likely' range (equivalent to 66 percent confidence limit) of $-1.7$ to $-0.3 W/m^2$ in IPCC report[6], our constraint on ERFaci reduces the uncertainty by about 57%.

We also show that models with a high ECS also have an exaggerated positive IHTC. Though there is a high correlation between ECS and $\beta_{PC1}$ in Fig. 3a, using emergent constraints to estimate the real-word ECS should result in a substantially lower value. This is because the $IHTC_{PC1}$ is also influenced by the cooling effect in AER, which suppresses the long-term warming due to GHG. More importantly, the observed IHTC is predominantly affected by AER and NAT, exhibiting a negative trend. That is, the observations and models are not in the same regime, hindering establishment of emergent constraints. Nevertheless, the models with low ECS tend to be more in line with the observations[35,36].

Recent studies indicate that the global mean surface temperature observed since 1970 offers limited insight into climate sensitivity and suggest that previous observational constraints[36] may skew estimates of the real-world ECS towards lower values[49]. Our present study suggests that these estimates remain valid when taking into account the SST pattern difference between the NH and SH since 1950. This follows because the modeled NH and SH SST warming rate is set by opposite surface wind speed trends in the two hemispheres (Fig. 4a and Supplementary Fig. 8a), in particular in the tropics and subtropics that cover 50% of the global surface. As such, the global warming rate, or equivalently, ECS, is affected by the surface wind speed. As expected, the trend of IHWC is correlated with the ECS (Supplementary Fig. 8c), indicating that models with high ECS possess a negative IHWC trend (and a positive IHTC trend, Supplementary Fig. 8a). In contrast, a few models with a positive IHWC trend are more in line with observations (with a negative IHTC trend), indicating a low ECS (less than 3.4 K) (Supplementary Fig. 8c).

### Implications for future tropical climate

Our study has so far suggested that the modeled response to AER aligns with the observed climate[23–25], whereas the modeled long-term response of IHTC and tropical climate is dominated by GHG and is not aligned with the observed climate. Models with lower ECS are closer to observations, though they still do not simulate the correct sign trend (except two models: #42 INM-CM4-8 and #33 GFDL-ESM4). In this section, we demonstrate the impact of models' sensitivity to GHG (equivalently, ECS) on future projections of tropical rainfall. A model with a higher ECS generally is associated with in an increased IHTC trend (Fig. 3a). The increased IHTC trend in turn enhances the northward shift of the ITCZ[2,22] (Fig. 5a).

Figure 5b, c examines the spatial rainfall responses from 2020 to 2070 compared to that of 1950-2014 in high and low ECS models, respectively. We select the CanESM5 (#19) and IPSL-CM6A-LR (#45) as high ECS models, and MIROC-ES2L (#50), MIROC6 (#51), and GISS-E2-1-G (#34) as low ECS models. All these models have an ensemble size of at least 30 members. Note that these models have an ERFaci close to the real-world estimation (Fig. 3b). Both sets of models predict a northward shift of the ITCZ under the Shared Socioeconomic Pathways 585 (SSP585) scenario. However, this shift is less pronounced in low ECS models, particularly in the Sahel-Amazon region. Similar results are also seen in the SSP245 scenario (Supplementary Fig. 12). A relatively smaller northward shift in the ITCZ, which is less disruptive of large-scale environment in the tropical Atlantic, could be associated with fewer Atlantic hurricanes[50,51], though many other factors can also influence hurricane frequency. In closing, we demonstrate that the observed and modeled hemispheric responses to external forcings differ substantially due to differences in their sensitivities. Future shifts in tropical climate are reliant on accurately quantifying both hemispheric differences in radiative forcing[52], as well as the hemispheric responses to these forcings.

## Discussion

Our analysis reveals a fundamental discrepancy between CMIP6 climate models and observations in simulating the interhemispheric thermal contrast since 1950. While models systematically show a positive IHTC trend driven primarily by greenhouse gas forcing, observations exhibit a negative trend dominated by anthropogenic aerosol and natural forcings. This model-data difference stems from an exaggerated GHG response mediated by wind-evaporation-SST feedback, which is particularly pronounced in high-ECS models.

These conclusions depend on separating the competing effects of GHG and AER by decomposing IHTC into long-term trend and multidecadal variability components, which exploit the distinct temporal evolution of forcing agents during 1950–2014. This period captures the era when anthropogenic forcings became substantial, while AER exhibited strong multidecadal variability that increased until ~1980 and then declined following clean air legislation. This temporal signature enables PCA to effectively separate the AER-dominated multidecadal variations ($IHTC_{PC2}$) from the long-term trend ($IHTC_{PC1}$), which is dominated by GHG in CMIP6 models.

Our sensitivity tests show robust results with ±10 years adjustments to the start year in the PCA decomposition, but the approach may not be suitable for other periods, in particular after 1980. After 1980, as AER emissions declined, both reduced AER cooling and continued GHG warming contributed to positive IHTC trends, compromising PCA's ability to isolate their individual effects. Nevertheless, the physical mechanism we identify, WES feedback amplifying the interhemispheric SST response to GHG, represents a robust process that operates across different time periods, even if the relative magnitude of GHG versus AER contributions varies.

https://doi.org/10.1038/s41467-026-69783-5

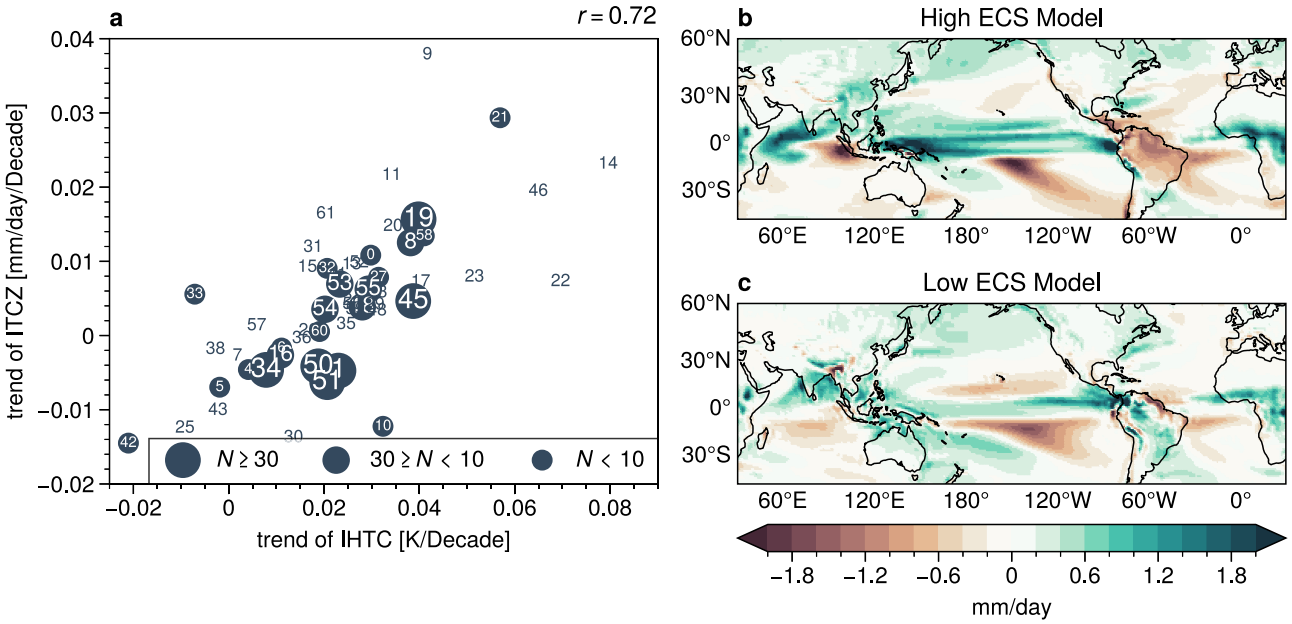


**Fig. 5 | Future projections of the intertropical convergence zone (ITCZ) in models with low and high equilibrium climate sensitivity (ECS). a** scatterplot illustrating the relationship between interhemispheric thermal contrast (IHTC) and ITCZ in CMIP6 models during 1950-2014. Numbers within each symbol correspond to individual CMIP6 models as listed in the legend of Fig. 3. **b** precipitation response in high ECS models for the period 2020–2070, relative to the climatology of 1950–2014. **c** As in **b**, but for low ECS models. Correlations in (**a**) are calculated using circled models, and they remain almost the same if using all models.

# Methods

## Definition of various metrics

The interhemispheric thermal contrast (IHTC) is defined as the SST difference between the NH[0–60°N] and the SH[40°S-0], a domain choice that maximizes data coverage quality while capturing the primary zones of hemispheric asymmetry. We exclude the Southern Ocean in the SH due to limited pre-satellite era observations. But including the Southern Ocean [60°S-0] does not change current results (Supplementary Fig. 1). SSTs are area weighted to calculate the IHTC. Cross-equatorial Hadley Circulation (HC) is defined as the averaged column mass streamfunction in [15°S-15°N]. Changing the domain does not affect the HC index as the streamfunction is largely uniform in the deep tropics (Supplementary Fig. 3). The Intertropical Convergence Zone (ITCZ) is the difference in precipitation between the Northern Hemisphere (0-30°N) and Southern Hemisphere (30°S-0)[25]. Note that observed rainfall is mainly over land, so the observed ITCZ represents the difference in land precipitation. The modeled ITCZ is also calculated over land to ensure a direct comparison with the observed data. The interhemispheric surface wind speed contrast (IHWC) is defined as the IHTC, but uses surface wind speed in place of SST.

## Observations

The SST trend and IHTC are calculated from the Extended Reconstructed Sea Surface Temperature version 5 dataset (ERSSTv5)[53] from the National Oceanic and Atmospheric Administration (NOAA), Centennial in situ Observation-Based Estimates (COBE)[54] SST2 data, and the Hadley Centre Sea Ice and SST dataset version 1.1 (HadISST)[55]. The cross-equatorial Hadley circulation and surface wind speed are calculated from the NOAA 20th-century reanalysis version 2[46], which only assimilates sea level pressure and SST. We specifically selected the 20th-century reanalysis because other reanalyses that assimilate air observations show biased Hadley Circulation responses[56]. The ITCZ is calculated from the Global Precipitation Climatology Centre (GPCC)[37], which covers only land but includes data for our entire study period, whereas precipitation data over the ocean is inadequate in the pre-satellite period.

## Model data

Model SSTs, precipitation, and wind were taken from the CMIP6[57] archive: https://esgf-node.llnl.gov/projects/cmip6/. The forced response as the ensemble mean was then calculated by averaging 542 ensemble members from the 57 models (Supplementary Data 1). We include as many CMIP6 model simulations as possible without cherry-picking. To quantify the internal variability, the first member (r1i1p1f1) of the pre-industrial control runs was also downloaded from 34 models. For pre-industrial control simulations, we first detrended the entire time series for each model to remove long-term drift. Next, we randomly selected a continuous 65-year time series and calculated its trend. This process was repeated 100 times for each model (with replacement), resulting in a total of 3400 realizations. We also obtained these variables from DAMIP[58] (https://damip.lbl.gov) to quantify the role of GHG (hist_GHG), AER (hist_aer), and NAT (hist_nat). All model data are linearly interpolated to a common grid (2°x1°, lat x lon). Model's ECS and ERFaci are taken from refs. 35,49.

## PCA

We conducted PCA onto the $IHTC_{GHG}$ and $IHTC_{AER}$ to remove their collinearity and identify the main patterns of variability in GHG and AER runs. The relationship between the $IHTC_{PC1}$, $IHTC_{PC2}$, $IHTC_{GHG}$, and $IHTC_{AER}$ could be represented in matrix form:

$$\begin{bmatrix} IHTC_{GHG} \\ IHTC_{AER} \end{bmatrix} = L \begin{bmatrix} IHTC_{PC1} \\ IHTC_{PC2} \end{bmatrix}$$

where $L$ is the loading matrix of the analysis that has been normalized to unit variance so $IHTC_{PC1}$ and $IHTC_{PC2}$ have unit $K$. Rewriting the equation above:

$$\begin{bmatrix} IHTC_{PC1} \\ IHTC_{PC2} \end{bmatrix} = L^{-1} \begin{bmatrix} IHTC_{GHG} \\ IHTC_{AER} \end{bmatrix}$$

where $L^{-1} = \begin{bmatrix} 0.708 & -0.706 \\ 0.706 & 0.708 \end{bmatrix}$. At face value, $IHTC_{PC2}$ is the sum of $IHTC_{GHG}$ and $IHTC_{AER}$. The long-term trends of $IHTC_{GHG}$ and $IHTC_{AER}$ cancel out because they have opposite signs, leaving the multidecadal variability dominated by AER. $IHTC_{PC1}$ is the difference between the $IHTC_{GHG}$ and $IHTC_{AER}$, primarily influenced by their long-term trends. The successful separation of the collinearity between $IHTC_{GHG}$ and $IHTC_{AER}$ in PCA results is due to the dominance of aerosols in the multidecadal IHTC in our study period. The PCA results are robust with +/-10 years of start year (e.g., 1940-2014), while the approach becomes less applicable if the period starts as early as 1900, prior to the rapid rise of the external forcing, or after 1980, since the Clean Air Act. Since 1980, the lack of multi-decadal variability in aerosols has led to both aerosols and greenhouse gases contributing to an increasing trend in IHTC. This makes it challenging for PCA to differentiate between their individual effects.

### Energy budget analysis for SST trend

We follow the methodology developed in ref. 59,60 to calculate the mixed layer energy budget and SST trend in model simulations. We start from the energy budget for the mixed layer:

$$\rho C_p H \frac{\partial T}{\partial t} = Q_{SW} + Q_{LW} + Q_{LH} + Q_{SH} + OHT$$

in which the tendency term on the left-hand side is the heat storage of ocean mixed layer. $\rho$, $C_p$, $H$, and $T$ are density of ocean, specific heat of ocean, mixed-layer depth of ocean, and mixed-layer temperature of ocean, respectively. The tendency term is fed by the energy uptake via net surface shortwave radiation $Q_{SW}$, net surface longwave radiation $Q_{LW}$, latent heat flux $Q_{LH}$, sensible heat flux $Q_{SH}$, and the convergence of ocean energy transports $OHT$, which includes oceanic processes across all scales and is not trivial to calculate using CMIP6 outputs. However, in the historical period, the heat storage tendency term is an order smaller than other terms on the right-hand side[34], such that neglecting the tendency term and calculating the linear trend of the energy equation above, we are able to estimate the $\Delta OHT$ as a residual:

$$0 = \Delta Q_{SW} + \Delta Q_{LW} + \Delta Q_{LH} + \Delta Q_{SH} + \Delta OHT$$

where the $\Delta$ denotes time tendency. The temperature dependence of latent heat could be linearized:

$$\Delta Q_{LH}^{T} = \alpha \bar{Q}_{LH} \Delta T$$

where $\alpha = \frac{L}{R_v T^2}$; $R_v = 461 J K^{-1} kg^{-1}$ is the gas constant for water vapor; $L = 2.5 \times 10^6 J/kg$ is the latent heat of evaporation. Other dependence of latent heat could be calculated as residual,

$$\Delta Q_{LH}^{others} = \Delta Q_{LH} - \Delta Q_{LH}^{T}$$

which is able to be further decomposed as in ref. 61 to attribute to changes in surface wind speed, relative humidity, and air-sea temperature difference.

Combine them together, we have a diagnostic equation for mixed layer temperature tendency, equivalent to SST tendency:

$$\Delta T = \frac{\Delta Q_{SW} + \Delta Q_{LW} + \Delta Q_{LH}^{others} + \Delta Q_{SH} + \Delta OHT}{\alpha \bar{Q}_{LH}}$$

Supplementary Fig. 8 shows that the NH and SH $\Delta T$ difference is dominated by the $\Delta Q_{LH}^{others}$ and $\Delta Q_{SH}$ term, which are driven by changes in air-sea temperature difference in high latitudes and surface wind speed in tropics and subtropics.

### Emergent constraints on ERFaci

Least-squares linear regressions are performed on the ERFaci and $\beta_{PC2}$. The probability density functions (PDFs) of the real-world ERFaci are then estimated based on the previously established framework[62].

## Data availability

Observed SST, rainfall and wind are taken from: ERSSTv5: https://psl.noaa.gov/data/gridded/data.noaa.ersst.v5.html COBE SST2: https://psl.noaa.gov/data/gridded/data.cobe2.html HadISST: https://www.metoffice.gov.uk/hadobs/hadisst/ GPCC Precipitation: https://psl.noaa.gov/data/gridded/data.gpcc.html NOAA 20th Century Reanalysis: https://psl.noaa.gov/data/gridded/data.20thC_ReanV2c.html All model data are taken from CMIP6 and DAMIP archive: https://esgf-node.llnl.gov/projects/cmip6/ and https://damip.lbl.gov.

## Code availability

The code to reproduce the results is archived at https://doi.org/10.5281/zenodo.17562106.

## References


1. Friedman, A. R., Hwang, Y.-T., Chiang, J. C. H. & Frierson, D. M. W. Interhemispheric temperature asymmetry over the twentieth century and in future projections. *J. Clim.* **26**, 5419–5433 (2013).
2. Sun, C., Li, J., Jin, F.-F. & Ding, R. Sea surface temperature interhemispheric dipole and its relation to tropical precipitation. *Environ. Res. Lett.* **8**, 044006 (2013).
3. Chen, Z. et al. Observationally constrained projection of Afro-Asian monsoon precipitation. *Nat. Commun.* **13**, 2552 (2022).
4. Kang, S. M., Held, I. M., Frierson, D. M. W. & Zhao, M. The response of the ITCZ to extratropical thermal forcing: idealized slab-ocean experiments with a GCM. *J. Clim.* **21**, 3521–3532 (2008).
5. Xue, J. et al. Divergent responses of extratropical atmospheric circulation to interhemispheric dipolar SST forcing over the two hemispheres in boreal winter. *J. Clim.* **31**, 7599–7619 (2018).
6. (IPCC), I. P. I. P. on C. C. *Climate Change 2021 - the Physical Science Basis*. (Cambridge University Press, 2023). https://doi.org/10.1017/9781009157896.
7. Friedman, A. R. et al. Forced and unforced decadal behavior of the interhemispheric sst contrast during the instrumental period (1881–2012): contexTUALIZING THE LATE 1960S–EARLY 1970S SHift. *J. Clim.* **33**, 3487–3509 (2020).
8. Xue, J. et al. Multidecadal variation of northern hemisphere summer monsoon forced by the SST inter-hemispheric dipole. *Environ. Res. Lett.* **17**, 044033 (2022).
9. He, C. et al. Tropical Atlantic multidecadal variability is dominated by external forcing. *Nature* **622**, 521–527 (2023).
10. Stouffer, R. J. et al. Investigating the causes of the response of the thermohaline circulation to past and future climate changes. *J. Clim.* **19**, 1365–1387 (2006).
11. McManus, J. F., Francois, R., Gherardi, J.-M., Keigwin, L. D. & Brown-Leger, S. Collapse and rapid resumption of Atlantic meridional circulation linked to deglacial climate changes. *Nature* **428**, 834–837 (2004).
12. Dickson, R. R., Meincke, J., Malmberg, S.-A. & Lee, A. J. The "great salinity anomaly" in the Northern North Atlantic 1968–1982. *Prog. Oceanogr.* **20**, 103–151 (1988).
13. Dima, M. & Lohmann, G. Evidence for two distinct modes of large-scale ocean circulation changes over the last century. *J. Clim.* **23**, 5–16 (2010).
14. Thompson, D. W. J., Wallace, J. M., Kennedy, J. J. & Jones, P. D. An abrupt drop in Northern Hemisphere sea surface temperature around 1970. *Nature* **467**, 444–447 (2010).

15. Manabe, S., Stouffer, R. J., Spelman, M. J. & Bryan, K. Transient responses of a coupled ocean–atmosphere model to gradual changes of atmospheric co2. part i. annual mean response. *J. Clim.* **4**, 785–818 (1991).
16. Stouffer, R. J., Manabe, S. & Bryan, K. Interhemispheric asymmetry in climate response to a gradual increase of atmospheric CO2. *Nature* **342**, 660–662 (1989).
17. Hutchinson, D., England, M., Santoso, A. & Hogg, A. Interhemispheric asymmetry in transient global warming: The role of Drake Passage. *Geophys. Res. Lett.* **40**, 1587–1593 (2013).
18. Marshall, J. et al. The ocean's role in polar climate change: asymmetric Arctic and Antarctic responses to greenhouse gas and ozone forcing. *Philos. Trans. R. Soc. A: Math., Phys. Eng. Sci.* **372**, 20130040 (2014).
19. Shokr, M. & Ye, Y. Why does arctic sea ice respond more evidently than antarctic sea ice to climate change? *Ocean-Land-Atmosphere Res.* **2**, 0006 (2023).
20. Armour, K. C., Marshall, J., Scott, J. R., Donohoe, A. & Newsom, E. R. Southern Ocean warming delayed by circumpolar upwelling and equatorward transport. *Nat. Geosci.* **9**, 549–554 (2016).
21. Xie, S.-P. Ocean warming pattern effect on global and regional climate change. *AGU Adv.* **1**, e2019AV000130 (2020).
22. Allen, R. J., Evan, A. T. & Booth, B. B. B. Interhemispheric aerosol radiative forcing and tropical precipitation shifts during the late twentieth century. *J. Clim.* **28**, 8219–8246 (2015).
23. Bonfils, C. J. W. et al. Human influence on joint changes in temperature, rainfall and continental aridity. *Nat. Clim. Chang.* **10**, 726–731 (2020).
24. Chung, E.-S. & Soden, B. J. Hemispheric climate shifts driven by anthropogenic aerosol–cloud interactions. *Nat. Geosci.* **10**, 566–571 (2017).
25. Hwang, Y., Frierson, D. M. W. & Kang, S. M. Anthropogenic sulfate aerosol and the southward shift of tropical precipitation in the late 20th century. *Geophys. Res. Lett.* **40**, 2845–2850 (2013).
26. Wang, C. Anthropogenic aerosols and the distribution of past large-scale precipitation change. *Geophys. Res. Lett.* **42**, 10,876–10,884 (2015).
27. Shi, J.-R., Wijffels, S. E., Kwon, Y.-O. & Xie, S.-P. Interhemispheric contrasts of ocean heat content change reveals distinct fingerprints of anthropogenic climate forcings. *Geophys. Res. Lett.* **50**, e2023GL102741 (2023).
28. Olonscheck, D. & Rugenstein, M. Coupled climate models systematically underestimate radiation response to surface warming. *Geophys. Res. Lett.* **51**, e2023GL106909 (2024).
29. Seager, R. et al. Strengthening tropical Pacific zonal sea surface temperature gradient consistent with rising greenhouse gases. *Nat. Clim. Chang.* **9**, 517–522 (2019).
30. Wang, C., Zhang, L., Lee, S.-K., Wu, L. & Mechoso, C. R. A global perspective on CMIP5 climate model biases. *Nat. Clim. Change* **4**, 201–205 (2014).
31. Wills, R. C. J., Dong, Y., Proistosecu, C., Armour, K. C. & Battisti, D. S. Systematic Climate Model Biases in the Large-Scale Patterns of Recent Sea-Surface Temperature and Sea-Level Pressure Change. *Geophys. Res. Lett.* **49**, e2022GL100011 (2022).
32. Zhang, S., Hu, Y., Zhang, J. & Xia, Y. Attribution of Biases of Interhemispheric Temperature Contrast in CMIP6 Models. *Adv. Atmos. Sci.* **41**, 325–340 (2024).
33. Lu, J. & Zhao, B. The role of oceanic feedback in the climate response to doubling CO2. *J. Clim.* **25**, 7544–7563 (2012).
34. Xie, S.-P. et al. Global warming pattern formation: sea surface temperature and rainfall. *J. Clim.* **23**, 966–986 (2010).
35. Wang, C., Soden, B. J., Yang, W. & Vecchi, G. A. Compensation between cloud feedback and aerosol-cloud interaction in cmip6 models. *Geophys. Res. Lett.* **48**, e2020GL091024 (2021).
36. Tokarska, K. B. et al. Past warming trend constrains future warming in CMIP6 models. *Sci. Adv.* **6**, eaaz9549 (2020).
37. Becker, A. et al. A description of the global land-surface precipitation data products of the Global Precipitation Climatology Centre with sample applications including centennial (trend) analysis from 1901–present. *Earth Syst. Sci. Data* **5**, 71–99 (2013).
38. Clement, A. C., Cane, M. A., Klavans, J. M., He, C. & Murphy, L. N. A signal-to-noise problem in model simulation of decadal climate modes. *J. Clim.* https://doi.org/10.1175/JCLI-D-25-0190.1 (2025)
39. Dong, Y., Kay, J. E., Deser, C., Capotondi, A. & Sanchez, S. C. Distilling the evolving contributions of anthropogenic aerosols and greenhouse gases to large-scale low-frequency surface ocean changes over the past century. *Geophys. Res. Lett.* **51**, e2024GL112020 (2024).
40. Xie, S.-P., Lu, B. & Xiang, B. Similar spatial patterns of climate responses to aerosol and greenhouse gas changes. *Nat. Geosci.* **6**, 828–832 (2013).
41. Wang, H., Xie, S.-P. & Liu, Q. Comparison of climate response to anthropogenic aerosol versus greenhouse gas forcing: distinct patterns. *J. Clim.* **29**, 5175–5188 (2016).
42. Haywood, J. M., Jones, A., Bellouin, N. & Stephenson, D. Asymmetric forcing from stratospheric aerosols impacts Sahelian rainfall. *Nat. Clim. Change* **3**, 660–665 (2013).
43. Zelinka, M. D. et al. Causes of higher climate sensitivity in CMIP6 models. *Geophys. Res. Lett.* **47**, e2019GL085782 (2020).
44. Shi, J.-R., Kwon, Y.-O. & Wijffels, S. E. Two distinct modes of climate responses to the anthropogenic aerosol forcing changes. *J. Clim.* **35**, 3445–3457 (2022).
45. Dagan, G., Stier, P. & Watson-Parris, D. Aerosol forcing masks and delays the formation of the North Atlantic warming hole by three decades. *Geophys. Res. Lett.* **47**, e2020GL090778 (2020).
46. Compo, G. P. et al. The twentieth century reanalysis project. *Q. J. R. Meteorological Soc.* **137**, 1–28 (2011).
47. Park, C., Soden, B. J., Kramer, R. J., L'Ecuyer, T. S. & He, H. Observational constraints suggest a smaller effective radiative forcing from aerosol–cloud interactions. *Atmos. Chem. Phys.* **25**, 7299–7313 (2025).
48. Smith, C. J. et al. Effective radiative forcing and adjustments in CMIP6 models. *Atmos. Chem. Phys.* **20**, 9591–9618 (2020).
49. Armour, K. C. et al. Sea-surface temperature pattern effects have slowed global warming and biased warming-based constraints on climate sensitivity. *Proc. Natl. Acad. Sci. USA* **121**, e2312093121 (2024).
50. Dunstone, N., Smith, D. M., Booth, B. B. B., Hermanson, L. & Eade, R. Anthropogenic aerosol forcing of Atlantic tropical storms. *Nat. Geosci.* **6**, 534–539 (2013).
51. Merlis, T. M., Zhao, M. & Held, I. M. The sensitivity of hurricane frequency to ITCZ changes and radiatively forced warming in aquaplanet simulations. *Geophys. Res. Lett.* **40**, 4109–4114 (2013).
52. Park, C. & Soden, B. Negligible contribution from aerosols to recent trends in Earth's Energy Imbalance. *Sci Adv* https://doi.org/10.21203/rs.3.rs-5679586/v1 (2025)
53. Huang, B. et al. Extended Reconstructed Sea Surface Temperature, Version 5 (ERSSTv5): Upgrades, Validations, and Intercomparisons. *J. Clim.* **30**, 8179–8205 (2017).
54. Hirahara, S., Ishii, M. & Fukuda, Y. Centennial-Scale Sea Surface Temperature Analysis and Its Uncertainty. *J. Clim.* **27**, 57–75 (2014).
55. Rayner, N. A. et al. Global analyses of sea surface temperature, sea ice, and night marine air temperature since the late nineteenth century. *J. Geophys. Res.: Atmos.* **108**, https://doi.org/10.1029/2002JD002670 (2003).
56. Chemke, R. & Polvani, L. M. Opposite tropical circulation trends in climate models and in reanalyses. *Nat. Geosci.* **12**, 528–532 (2019).

57. Eyring, V. et al. Overview of the Coupled Model Intercomparison Project Phase 6 (CMIP6) experimental design and organization. *Geoscientific Model Dev.* **9**, 1937–1958 (2016).
58. Gillett, N. P. et al. The Detection and Attribution Model Intercomparison Project (DAMIP v1.0) contribution to CMIP6. *Geoscientific Model Dev.* **9**, 3685–3697 (2016).
59. Kang, S. M. et al. Global impacts of recent Southern Ocean cooling. *Proc. Natl. Acad. Sci.* **120**, e2300881120 (2023).
60. Hwang, Y.-T., Xie, S.-P., Deser, C. & Kang, S. M. Connecting tropical climate change with Southern Ocean heat uptake. *Geophys. Res. Lett.* **44**, 9449–9457 (2017).
61. He, C. et al. A North Atlantic warming hole without ocean circulation. *Geophys. Res. Lett.* **49**, e2022GL100420 (2022).
62. Cox, P. M., Huntingford, C. & Williamson, M. S. Emergent constraint on equilibrium climate sensitivity from global temperature variability. *Nature* **553**, 319–322 (2018).

## Acknowledgements

The authors appreciate insightful discussions with Drs. Anthony Broccoli, Susan Wijffels, Shang-Ping Xie, and Shawn Wang. We acknowledge climate modeling groups for producing model outputs and the Program for Climate Model Diagnosis and Intercomparison for maintaining the CMIP6 data archive from which we drew the data. The authors acknowledge support for this work from NOAA Grant NA20OAR4310400, NSF Climate and Large-Scale Dynamics Grants AGS 1735245 and AGS 1650209, NSF P2C2 Grant AGS 1703076, and NSF Physical Oceanography Program Grant OCE-2048336. C.H. is supported by the Woods Hole Oceanographic Institute Weston Howland Jr. Postdoctoral Fellowship and Northeastern University. The authors also acknowledge high-performance computing support from Derecho (doi:10.5065/D6RX99HX) carried on NCAR's Computational and Information Systems Laboratory.

## Author contributions

C.H. conceived this study, performed the analysis, and wrote the paper; C.H., A.C., M.C., A.G., Y.K., J.S., J.K., and L.M. discussed the results and contributed to the manuscript.

## Competing interests

The authors declare no competing interests.

## Additional information

**Supplementary information** The online version contains supplementary material available at https://doi.org/10.1038/s41467-026-69783-5.

**Correspondence** and requests for materials should be addressed to Chengfei He.

**Peer review information** *Nature Communications* thanks Jiankai Zhang and the other anonymous reviewer(s) for their contribution to the peer review of this work. A peer review file is available.